JMEPEG
https://doi.org/10.1007/s11665-024-09499-z

1059-9495/$19.00

ORIGINAL RESEARCH ARTICLE

Dislocation-Based Finite Element Modeling of an Off-Axis Twist Extrusion with Variable Helix Angles

Moeen Barkhordari and Majid Seyed-Salehi

Submitted: 24 September 2023 / Revised: 23 February 2024 / Accepted: 18 March 2024

This study presents a comprehensive investigation into the deformation behavior and microstructural characteristics of pure aluminum during off-axis twist extrusion with variable helix angle. To accurately predict the material's deformation characteristics, a combined finite element and modified ETMB (Estrin–Toth–Molinari–Brechet) dislocation-based constitutive model is employed. The modified ETMB model is rigorously validated against experimental observations, demonstrating its reliability and relevance in capturing the complex deformation mechanisms. Moreover, the effects of extrusion conditions and die geometry on the deformation characteristics, dislocation distribution, cell structure, and material strength are analyzed. The results show that the die geometry parameters, such as twist angle, off-axis parameter, and twist zone length, significantly influence the material's deformation behavior. Increasing the twist angle and off-axis parameter leads to a higher extrusion load and mean equivalent plastic strain while increasing the twist zone length reduces the extrusion load and plastic strain. The study also highlights the role of backward pressure in achieving better die filling and eliminating gaps between the workpiece and the die. The increase in backward pressure leads to a higher extrusion load and mean equivalent plastic strain. The findings enhance the understanding of the TE process and pave the way for optimizing material processing to achieve desired microstructural properties.

Keywords dislocation-based constitutive model, finite element method, modified ETMB dislocation model, off-axis twist extrusion, severe plastic deformation

1. Introduction

In polycrystalline materials, grain size and morphology affect the various aspects of physical and mechanical properties as well as chemical behaviors and corrosion resistances (Ref 1, 2). In recent years, nanostructured and ultrafine grain (UFG) materials have attracted significant interest due to their proper properties (Ref 3). One of the most effective processing approaches to produce contamination- and porosity-free UFG metallic materials is the severe plastic deformation (SPD) technique (Ref 3-5). From the 1950s until today, several SPD methods have been developed, e.g., equal-channel angular pressing/extrusion (ECAP/ECAE) (Ref 6-9), high-pressure torsion (HPT) (Ref 10, 11), multi-directional forging (MDF) (Ref 12), twist extrusion (TE) (Ref 13-17), hydrostatic extrusion (HE) (Ref 18, 19), constrained groove pressing and rolling (CGP and CGR) (Ref 20, 21), accumulative roll bonding (ARB) (Ref 22), continuous conshearing ECAP (CC-ECAP) (Ref 23), cyclic extrusion compression (CEC) (Ref 24), simple shear extrusion (SSE) (Ref 25) and tube channel pressing (TCP) (Ref 26). In these methods, the grain refinement depends on the deformation regime during the SPD and the initial microstructure (Ref 27, 28).

Moeen Barkhordari and **Majid Seyed-Salehi**, Faculty of Materials Science and Engineering, K. N. Toosi University of Technology, Tehran 1969764499, Iran. Contact e-mail: seyedsalehi@kntu.ac.ir.

It is generally accepted that the mechanisms of grain refinement include the formation of dislocation cells, followed by the transformation of cell walls into low-angle grain boundaries, and subsequently conversion to large-angle grain boundaries by increasing the misorientations angle of boundaries. In this phenomenon, the dislocation cell structure acts as a precursor of the final grain structure after SPD processes (Ref 29).

The TE technique has been proposed by Beygelzimer et al. (Ref 13) for grain refinement of metals. In this method, the twist die can be easily installed on the extrusion equipment (Ref 30, 31), and the specimen twists around the extrusion axis to a given angle, whereas the shape and dimensions of the specimen after the process are similar to the initial ones. So, the process can be repeated and consequently apply a severe shear plastic strain on the specimen to achieve a UFG material (Ref 16). Theoretically, the conventional TE method is suitable for processing prismatic samples with a non-circular profile. It seems that the round bars cannot be extruded with the TE technique. Wang et al. (Ref 32, 33) proposed a hybrid TE technique named elliptical cross-section spiral equal-channel extrusion (ECSEE) to impose severe plastic shear strains on the round bars. In this method, the extrusion die consists of a round-ellipse cross-section transitional channel at the inlet followed by a twist extrusion channel with an elliptical profile and an ellipse-round cross-section transitional channel at the exit. In 2003, Beygelzimer et al. (Ref 34) proposed the concept of the off-axis twist extrusion (OTE) technique for processing the round bars. They later conducted a detailed analysis of the OTE process in 2015 (Ref 35). In this technique, the twist axis is parallel with and displaced from the central axis of the round bar. The experimental and numerical analysis of deformation in OTE with constant helix angle shows the simple shear deformation during the process at the inlet and exit planes of the die channel.

Published online: 30 April 2024

The use of FE simulations and dislocation-based modeling has gained significance in investigating metal forming processes. In dislocation density models, the total density of dislocations is considered as an internal variable of the material, and the dislocation evolution is supposed to be a function of the deformation states and history. These models can be used to predict the flow stress and microstructural characteristics (dislocations and cell structures, grain and sub-grain morphology) of materials during plastic deformation (Ref 36, 37). Estrin et al. (Ref 36) proposed a general dislocation-based model known as the ETMB (Estrin–Toth–Molinari–Brechet) model for large strain deformations. In this model, the deformed single-phase material is assumed to be composed of cells and cell walls. The model describes the evolution of dislocation density within cell walls and cell interiors, considering dislocation multiplication, annihilation, and migration mechanisms. Toth et al. (Ref 37) extended a 3D ETMB model and implemented a viscoplastic self-consistent polycrystal model to predict flow curves in different loading paths. Parvin et al. (Ref 38) further improved the ETMB model by incorporating the effects of stacking fault energy on dislocation annihilation. The ETMB model was employed to predict the dislocation structure in different SPD processes. The evolution of dislocation structure and mechanical properties of copper (Ref 39, 40), aluminum (Ref 39, 41), and tantalum (Ref 42) during the ECAP process were modeled using a hybrid approach based on the flow function and the ETMB model. Also, a kinematically admissible streamline was coupled with the ETMB model to predict the dislocation cell structure during the ECAE process (Ref 43). Romanov et al. (Ref 44) used a combination of the ETMB model and a statistical crystal plasticity constitutive model to simulate the grain refinement of copper during ECAP at room temperature. The study suggests that explicitly considering cell rotation in the model is crucial for accurately describing the grain fragmentation mechanism. Also, the cell/grain refinement during the severe shot peening process of a high-strength low-alloy steel was simulated using a combination of FE and ETMB models (Ref 45). Sheikh et al. (Ref 25) employed a combination of crystal plasticity FE and a modified ETMB models to simulate the effects of strain reversal on the evolution of texture and microstructure in SSE processing.

In this study, the material deformation of fully annealed pure aluminum in an OTE die with an off-centric circular cross section with a variable helix angle has been investigated. In this method, the circular die cross section remains unchanged along the twist axis of the die, as schematically illustrated in Fig. 1. Moreover, the effects of geometric variables of the OTE die, and the extrusion process conditions (backward pressure) have been studied. The modified ETMB model has been employed to investigate the evolution of the dislocation density inside cells and cell walls and finally to predict the total dislocation density and the material flow stress.

2. Modeling

This paper presents a simulation of the OTE with a circular die cross section using a combined FE and ETMB model, which is discussed in section 2.1. Additionally, the extrusion die design and surface meshing were based on the model described in section 2.2. As plastic strain and dislocation

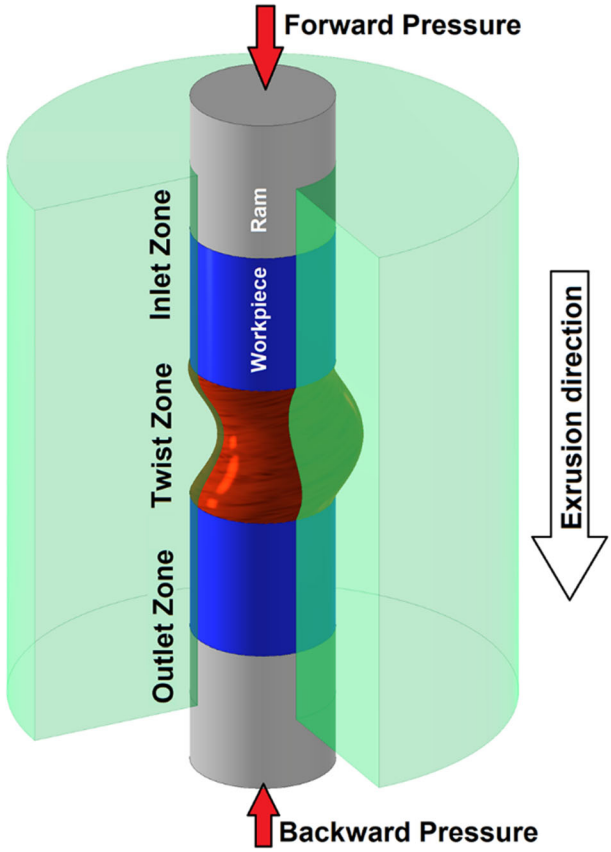

Fig. 1 Three-quarter section view of the OTE die with off-centric circular die cross section

structure are distributed non-homogenously in severe plastic deformation (SPD) processes (Ref 25-27), a dislocation-based constitutive model was employed to simulate the deformation behavior and cell refinement of the material during the OTE process. This model considers different mechanisms for dislocation accumulation and annihilation inside the cells and cell walls, considering the stacking fault energy and the temperature effect (section 2.3).

2.1 FE Modeling

In this study, a nonlinear three-dimensional explicit FE method is employed to simulate the deformation of fully annealed pure aluminum during the OTE process. The workpiece, a cylinder with a cross-section radius of 15 mm and a height of 90 mm, was subjected to forward and backward pressures using two rigid plates as punches. The workpiece was discretized using three-dimensional 8-node hexahedral elements with the reduced integration formulation (element type C3D8R in the Abaqus package). Also, three-dimensional 4-node rigid elements (element type R3D4 in the Abaqus package) were used for the rigid plates and die surface. The simulation included separable tangential contact between the workpiece and the die, as well as the workpiece and the punches. The effects of the geometrical characteristics of the OTE die (including twist angle, off-axis parameter, and twist zone length) and process parameters (backward pressure) on the deformation behavior of the workpieces, dislocation density, and cell size distribution during the OTE process were investigated.

2.2 Extrusion Die

The extrusion die is composed of three zones, namely the inlet, twist, and outlet zones, as illustrated in Fig. 1. The inlet and outlet die zones are two cylindrical cavities with the same cross-sectional diameter. The die surface in the twist zone is formed by moving along and simultaneously rotating an off-center circular cross section around the die axis perpendicular to the cross section. The off-center circular cross section is shown schematically in Fig. 2(a), where the full-line circle denotes the die cross section at the inlet, and the dashed circle represents the die cross section rotated by an angle of θ relative to the inlet cross section along the extrusion axis (the vector perpendicular to the plane of paper passes through origin "o"). In this figure, the parameter " a" denotes the off-axis.

In the twist zone, each point on the die cross section rotates slightly around the z-axis by an angle $\delta\theta$ as it moves along the extrusion axis (z-axis) by a distance of δz, as illustrated in Fig. 2(b). Accordingly, the following Eq. can be written:

$$\tan\beta = \frac{R\delta\theta}{\delta z} \quad \text{(Eq 1)}$$

where β is the helix angle and R is the distance between point " A" and the extrusion axis (z). The twist angle (θ) can be obtained by integrating Eq. 1 along the extrusion axis (z) from 0 to z, as shown in Eq. 2:

$$\theta(z) = \int_0^z \frac{\tan\beta}{R}\mathrm{d}\xi \quad \text{(Eq 2)}$$

The helix angle β can be constant or vary along the extrusion axis. In this study, a linear relationship between β and z is assumed, as given by Eq. 3.

$$\beta = \begin{cases} \beta_0 + \dfrac{\beta_l - \beta_0}{l} & z < l \\ \beta_l + \dfrac{\beta_L - \beta_l}{L - l}(z - l) & z \geq l \end{cases} \quad \text{(Eq 3)}$$

where L is the length of the twist zone and β_0 and β_L are the helix angles at the inlet and outlet of the twist zone, respectively. In this equation, β_l is the maximum helix angle at l from the inlet zone. Fig. 3 schematically shows the helix and twist angles as functions of z (in this figure for instance $\beta_0 = 15°, \beta_l = 80° and \beta_L = 30°$).

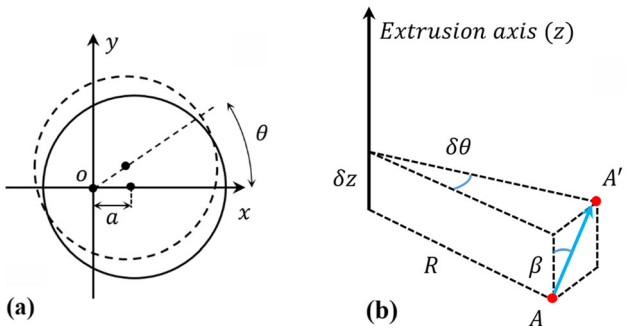

Fig. 2 Schematic illustration of (a) rotation of the circular off-centric cross section (The dashed circle shows the die cross section rotated by θ along the extrusion axis) and (b) moving and rotating a surface point on the die cross section along the extrusion axis

By substituting Eq. 3 into Eq. 2, the twist angle can be expressed as a function of die length as follows:

$$\theta(z) = \begin{cases} \dfrac{-l}{R(\beta_l - \beta_0)}\ln\left(\dfrac{\cos(\beta)}{\cos(\beta_0)}\right) z \leq l \\ \theta_l - \dfrac{L - l}{R(\beta_L - \beta_l)}\ln\left(\dfrac{\cos(\beta)}{\cos(\beta_l)}\right) z > l \end{cases} \quad \text{(Eq 4)}$$

where θ_l can be determined by the following equation:

$$\theta_l = \frac{-l}{R(\beta_l - \beta_0)}\ln\left(\frac{\cos(\beta_l)}{\cos(\beta_0)}\right) \quad \text{(Eq 5)}$$

The die surface meshes were generated using a MATLAB subroutine based on the above equations. This method provides precise meshing with consistent shapes and sizes, even in the twist zone. In this study, it is assumed that the helix angles in the inlet and outlet of the twist zone are zero. As a result, the workpiece enters and exits the die smoothly, and shear deformation is gradually applied to the material along the twist zone by changing the helix angle.

2.3 Dislocation Model

Experimental studies have demonstrated that the density and the structure of dislocations significantly change during SPD processes (Ref 6, 24, 26, 42, 46). To model the evolution of dislocations during SPD, it is generally assumed that the dislocation structure in large strains comprises two parts: the cell interior and cell walls (Ref 47, 48). The competition between work hardening and dynamic recovery determines the dislocation structures inside the cells and cell walls. The mechanisms i.e., dislocation multiplication, dislocation migration between the cell interior and the walls, and dislocation annihilation due to recovery change the dislocation density in cells or walls (Ref 36). By applying a shear strain increment " $d\gamma$", dislocations migrate from the cell walls toward the cell interior (Ref 37). As a result, the dislocation density in the cell interior is increased as follows (Ref 38)

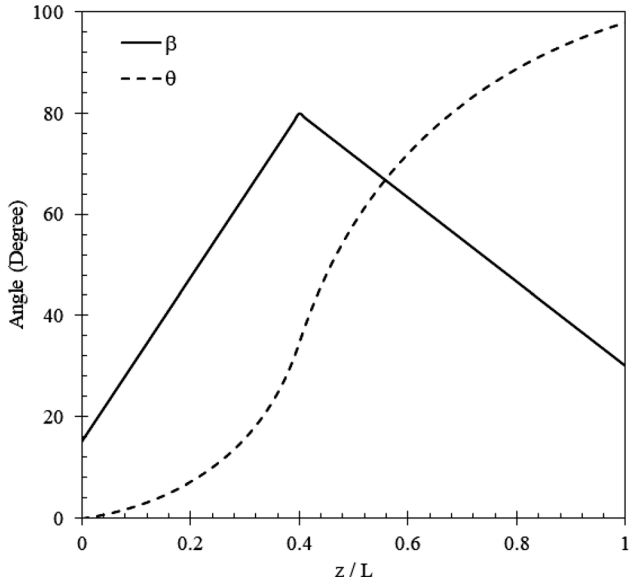

Fig. 3 Schematic graph of helix (β) and twist (θ) angles as functions of z ($\beta_0 = 15°, \beta_l = 80°$ *and* $\beta_L = 30°$)

$$\frac{d\rho_c{}^{+}}{d\gamma} = \frac{\alpha^*\sqrt{\rho_w}}{\sqrt{3}b} \quad \text{(Eq 6)}$$

where ρ_w and ρ_c are the dislocation density in the cell walls and cell interior, respectively. b is the length of the Burgers vector, and α^* represents the fraction of dislocations migrated from the cell walls toward the cell interior. On the other hand, the migration of dislocations from the cell interiors toward the walls and the annihilation of dislocations due to dynamic recovery decrease the dislocation density of the cell interiors. By applying plastic shear strain, a fraction of dislocations inside the cells leave the cells and join the cell walls. This phenomenon can increase the dislocation density on the walls and, conversely, decrease the dislocation density inside the cells. The loss rate of cell dislocations is given by the first term in Eq. 7, where β^* is the fraction of cell dislocation that leaves the cell interior (Ref 37). The second term represents the loss rate of cell interior dislocations due to the dislocation annihilation by dynamic recovery, mainly controlled by the cross-slip of dislocations at low temperatures (Ref 38, 49).

$$\frac{d\rho_c{}^{-}}{d\gamma} = \frac{6\beta^*}{\mathrm{bd}(1-f)^{1/3}} + \frac{1}{\dot{\gamma}}\left(\frac{Gb^4\rho_c v_D}{8\pi\Gamma V}\exp\left(-A\,\ln\left(\frac{Gb^4 v_D}{16\pi\Gamma V\dot{\gamma}}\right) + \frac{\alpha\sqrt{\rho_c}V}{b^2}\right)\right) \quad \text{(Eq 7)}$$

where d is the average cell size, $\dot{\gamma}$ is the applied shear strain rate, G is the shear elastic modulus, v_D is Debye frequency, Γ is the stacking fault energy, V is the activation volume for cross-slip, and A and α are material constants. In this equation, f denotes the volume fraction of cell walls, which is a function of applied resolved shear strain γ (Ref 37)

$$f = f_\infty + (f_0 - f_\infty)\exp(-\eta\gamma) \quad \text{(Eq 8)}$$

where f_0 and f_∞ are the initial and the saturation volume fraction of cell walls, respectively, and η is the model constant. Eq. 9 presents the increase in the dislocation density of cell walls. The first term of Eq. 9 represents the rate of dislocation generation on the cell walls due to the activation of Frank-Read sources. The second term shows the rate of dislocation aggregation due to dislocation migration from cell interiors to cell walls during deformation (Ref 37, 38).

$$\frac{\mathrm{d}\rho_w{}^{+}}{\mathrm{d}\gamma} = \frac{\sqrt{3}\beta^*(1-f)\sqrt{\rho_w}}{\mathrm{bf}} + \frac{6\beta^*(1-f)^{2/3}}{\mathrm{bdf}} \quad \text{(Eq 9)}$$

It is important to note that the cell wall dislocations can be subdivided into statistically stored (SSDs) and geometrically necessary dislocations (GNDs). The geometrically necessary dislocations contribute to Burgers vector imbalance in cell walls and lead to boundary misorientation across cell walls (Ref 50). The evolution of the density of GNDs in cell walls can be derived by considering a fraction (ξ_1) of dislocation generated by Frank-Read mechanisms and a fraction (ξ_2) of migrated dislocation from cell interiors to the walls (Ref 51, 52). Therefore, the density of GNDs in the cell walls is increased as follows

$$\frac{\mathrm{d}\rho_{wG}{}^{+}}{\mathrm{d}\gamma} = \xi_1\frac{\sqrt{3}\beta^*(1-f)\sqrt{\rho_w}}{\mathrm{bf}} + \xi_2\frac{6\beta^*(1-f)^{2/3}}{\mathrm{bdf}} \quad \text{(Eq 10)}$$

where ρ_{wG} is the density of GNDs in cell walls. The wall misorientation Θ can be derived from the following equation.

$$\Theta = \tan^{-1}\left(b\sqrt{\rho_{wG}}\right) \quad \text{(Eq 11)}$$

The recovery phenomenon by dislocation climb mechanisms on the walls causes a decrease in the dislocation density (Ref 53, 54), which is demonstrated by Eq. 12 (Ref 38) as follows:

$$\frac{\mathrm{d}\rho_w{}^{-}}{\mathrm{d}\gamma} = \frac{8\alpha v_D n_c}{\dot{\gamma}\delta}\left(\frac{24\pi(1-\upsilon)\Gamma}{G(2+\upsilon)}\right)^2\exp\left(\frac{-U}{RT}\right)\left[\exp\left(\frac{\Omega\tau^*}{k_B T}\right) - 1\right]\rho_w^2 \quad \text{(Eq 12)}$$

where n_c is the coordination number for atomic diffusion, υ is the Poisson's ratio, U is the activation energy of self-diffusion, Ω is the atomic volume, τ^* is the stress acting on the dislocation pile-up, and k_B is Boltzmann constant. Accordingly, the evolution of the dislocation density of the cells and cell walls can be derived by subtracting Eq. 7 from Eqs. 6 and 12 from Eq. 9, respectively.

$$\frac{\mathrm{d}\rho_w}{\mathrm{d}\gamma} = \frac{\mathrm{d}\rho_w{}^{+}}{\mathrm{d}\gamma} - \frac{\mathrm{d}\rho_w{}^{-}}{\mathrm{d}\gamma} \quad \text{(Eq 13)}$$

$$\frac{\mathrm{d}\rho_c}{\mathrm{d}\gamma} = \frac{\mathrm{d}\rho_c{}^{+}}{\mathrm{d}\gamma} - \frac{\mathrm{d}\rho_c{}^{-}}{\mathrm{d}\gamma}$$

The dislocation density during the deformation can be obtained by integrating the above equations along the strain path. Using Euler's explicit integration method, the dislocation density in the cells and the cell walls can be calculated by applying the shear strain increment $\delta\gamma$ at each time step as follows:

$$\begin{aligned}\rho_w^{(t+\delta t)} &= \rho_w^{(t)} + \left(\frac{\mathrm{d}\rho_w{}^{+}}{\mathrm{d}\gamma} - \frac{\mathrm{d}\rho_w{}^{-}}{\mathrm{d}\gamma}\right)^{(t)}\delta\gamma \\ \rho_c^{(t+\delta t)} &= \rho_c^{(t)} + \left(\frac{\mathrm{d}\rho_c{}^{+}}{\mathrm{d}\gamma} - \frac{\mathrm{d}\rho_c{}^{-}}{\mathrm{d}\gamma}\right)^{(t)}\delta\gamma\end{aligned} \quad \text{(Eq 14)}$$

The total dislocation density, denoted as ρ_t, can be estimated using Eq. 15.

$$\rho_t = f\rho_w + (1-f)\rho_c \quad \text{(Eq 15)}$$

Considering the dislocation density in the cells and the cell walls, the average cell size can be derived, as shown in Eq. 16 (Ref 38, 53).

$$\mathrm{d} = \frac{K_0 + K_1\exp(-\gamma/\kappa)}{\sqrt{\rho_t}} \quad \text{(Eq 16)}$$

In the above equation, K_0, K_1, and κ are the model constants. Using the Taylor model (Ref 36, 38), the flow stress can then be calculated as follows:

$$\sigma = M\alpha Gb\sqrt{\rho_t} \quad \text{(Eq 17)}$$

where M is the Taylor factor. The model constants and variables for pure aluminum are presented in Table 1.

3. Results and Discussion

3.1 Dislocation Modeling

Based on the presented dislocation model, the change of total dislocation density relative to plastic strain, strain rate, and temperature for pure aluminum is illustrated in Fig. 4. As can be seen, the accumulation rate of total dislocation density is highest at low strains, but it decreases continuously with

increasing strains. The rate of dislocation annihilation is directly related to the dislocation density, as can be seen in Eqs 7 and 12. By applying plastic strain, the dislocation density in cell interiors and the walls increases, which leads to an increase in the driving force for recovery mechanisms, such as climb and cross-slip of dislocations (Ref 55). Consequently, the increase in the work-softening rate slows down the accumulation rate of the dislocations at severe strains. Also, the effect of deformation temperature on dislocation density is shown in Fig. 4(a). As can be seen, the rate of dislocation accumulation decreases by increasing the temperature. Dislocation climb is a thermally activated phenomenon (Ref 55) (consider Eq. 12), and it controls the dynamic recovery in the cell walls. Increasing the deformation temperature speeds up the dislocation climb and consequently results in a decrease in the dislocation density. The effect of strain rate on the evolution of the dislocation density is presented in Fig. 4(b). Dislocation annihilation is inversely proportional to the shear strain rate (Eq. 7 and 12). Increasing the strain rate decreases the rate of dislocation annihilation in the cell interiors and walls.

The evolution of dislocation cells during the plastic deformation is depicted in Fig. 5. As can be seen, at the early

Table 1 The model parameters and the material constants of the dislocation model (Ref 38, 51)

Parameter	Value
α^*	2.4×10^{-3}
β^*	5.4×10^{-3}
b(m)	2.86×10^{-10}
υ	0.33
M	3.06
Γ, J/m^2	0.166
Ω	b^3
n_c	11
f_∞	0.06
f_0	0.25
η	0.46
δ	5
α	0.25
A	1.05
K_0	16.5
K_1	25
κ	3.85
V	$300\ b^3$
G, GPa	25
ν_D, Hz	10^{13}
ρ_c(Initial value), m/m^3	10^{13}
ρ_w(Initial value), m/m^3	10^{14}
U, kJ/mol	120
ξ_1	0.1
ξ_2	0.05

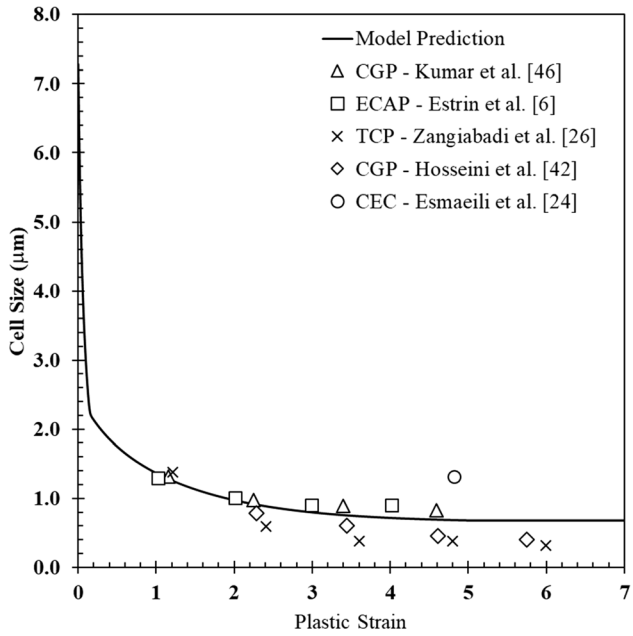

Fig. 5 Evolution of dislocation cell during the plastic deformation compared with the experimental results of pure aluminum (Ref 6, 24, 26, 42, 46)

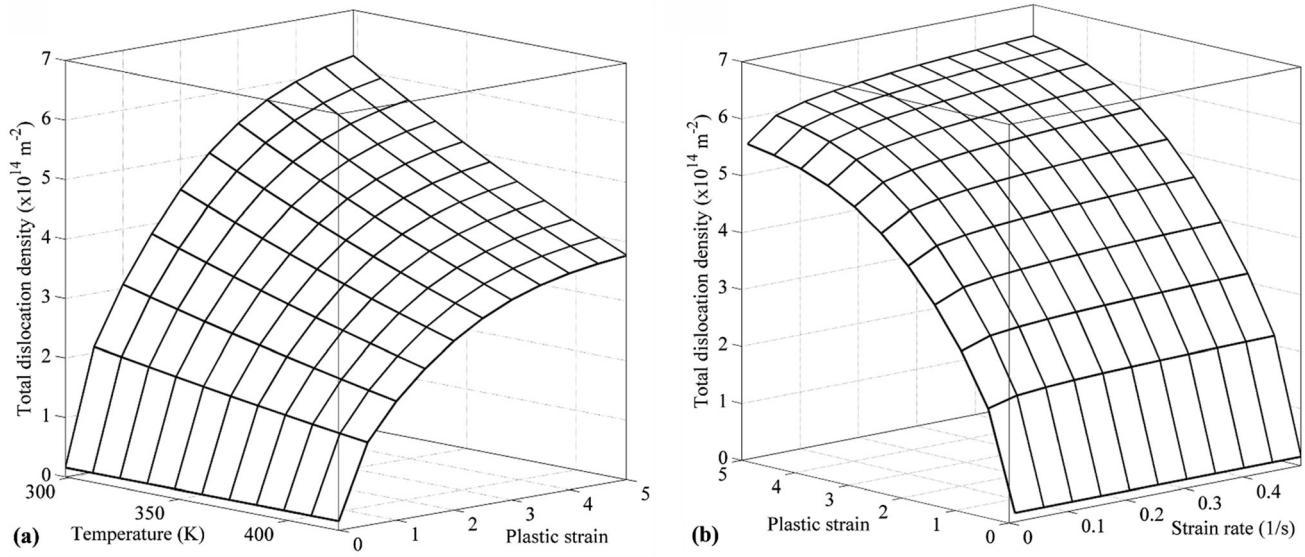

Fig. 4 The total dislocation density in pure aluminum as a function of (a) deformation temperature and plastic strain at the strain rate of 0.2 s^{-1} and (b) strain rate and plastic strain at 298 K

stages of deformation, there is a rapid decrease in cell size, followed by a slower reduction until a plateau at higher strains. By applying the plastic strain, the dislocation density increases, causing a decrease in cell size (see Eq. 12, which shows the dependency of cell size on the dislocation density in cells and cell walls). This behavior is in agreement with previous studies (Ref 38, 54) and the reported experimental data (Ref 6, 24, 26, 42, 46), which can be seen in Fig. 5. In this figure, the model predictions compared to the experimental results from studies on a high purity (Ref 6, 24, 46) and a commercial purity aluminum (Ref 26, 42) severely deformed by CGP (Ref 42, 46), ECAP (Ref 6), CEC (Ref 24) and TCP (Ref 26) processes. In these studies, the grain refinement was evaluated using transmission electron microscope (TEM) (Ref 6, 42) and x-ray diffraction analysis employing Williamson–Hall method (Ref 24, 26, 42, 46). The quantitative comparison between experimental data and model predictions shows a reasonable agreement.

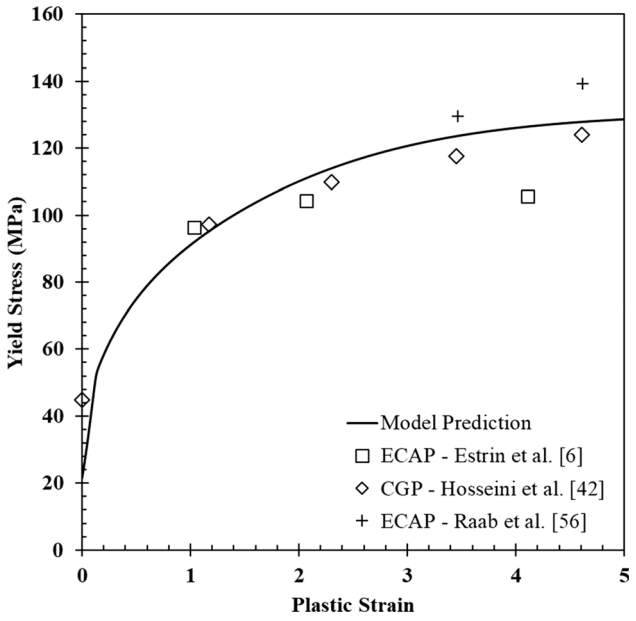

Fig. 6 The flow stress of pure aluminum severely deformed in 298 K and strain rate of 0.2 s^{-1} compared with the experimental results (Ref 6, 42, 56)

The variation of flow stress as a function of the cumulative plastic strain is presented in Fig. 6. The predicted results show reasonable consistency compared with the experimental data reported in previous studies using CGP (Ref 42) and ECAP (Ref 6, 56) processes. The observed variation in flow stress among experimental studies may be attributed to differences in the SPD methods, chemical compositions, and initial states of materials employed by different researchers.

3.2 Deformation Analysis

Fig. 7 illustrates the material flow and velocity distribution at different cross sections of the die (i.e., at the inlet, 1/4, middle, ¾, and outlet of the twist zone) during TE. By pushing the workpiece into the twist zone, the material spirally twists in the die cavity, as shown in the figure. During extrusion, surface tractions and contact pressure in the opposite moving direction increase the internal pressure in the twist zone. However, during the OTE process, as the material moves forward through the die cavity, it resists rotating along with the die surface cross section, resulting in the formation of a gap between the die surface and the material. In this figure, the space between the material and the red circle at each cross section indicates the

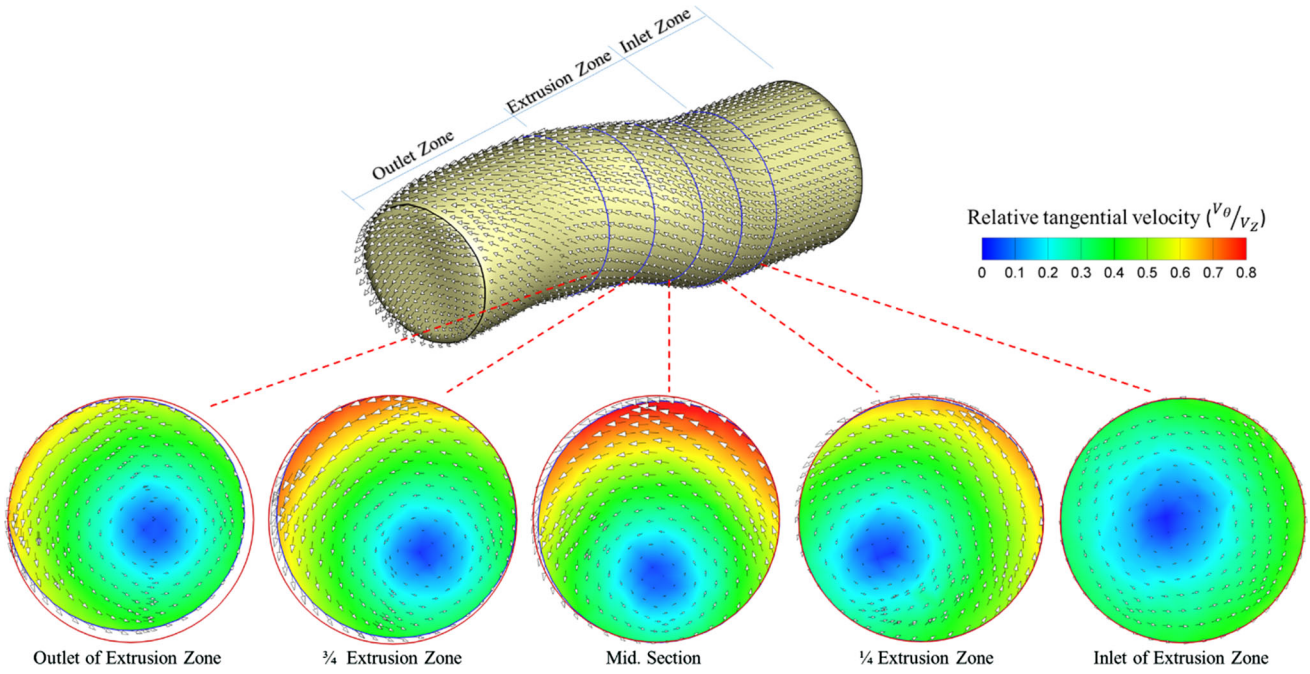

Fig. 7 The material flow and velocity distribution at the inlet, 1/4, middle, ¾, and outlet of the twist zone during OTE, with a twist angle of 180° and no backward pressure. The colorful contour represents the relative tangential velocity ((V_θ/V_Z), V_θ, and V_Z are the tangential velocity at each cross section and extrusion velocity, respectively)

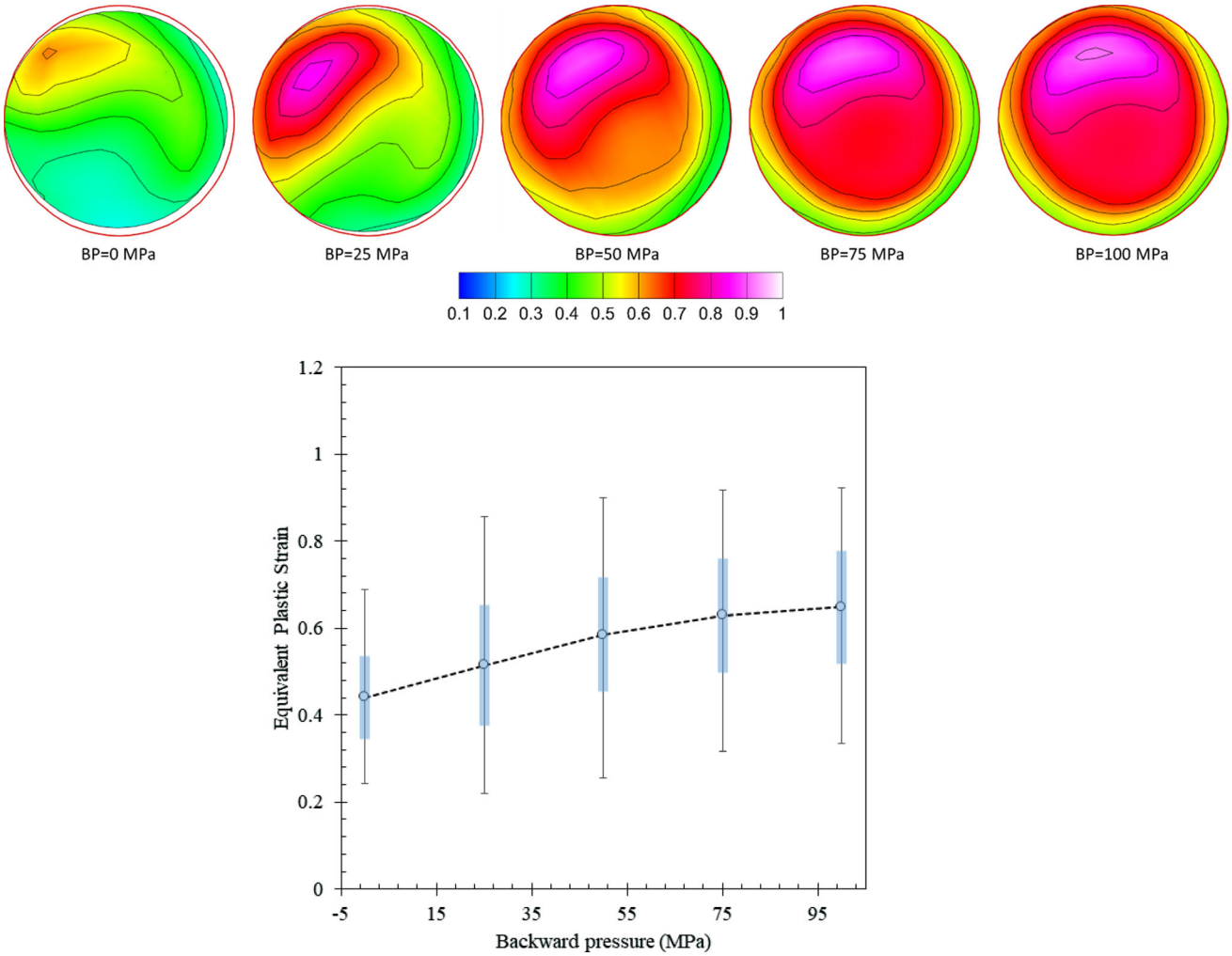

Fig. 8 (a) Distribution of equivalent plastic strain in outlet zone after OTE with different backward pressure with a twist angle of 180° and (b) variation of mean, deviation, and range of equivalent plastic strain with backward pressure (The candlestick at each point demonstrates the standard deviation and data range)

workpiece-die gap (where the red circle represents the die surface cross section). The separation between the die and workpiece depends on the die geometry and backward pressure, which will be discussed in the following sections.

Keeping the original shape of the workpiece after the process and a complete fill of the die cavity during extrusion are both desired characteristics of the OTE process. Backward pressure is an effective variable for eliminating the gap between the die and the workpiece. Applying the backward pressure increases the radial forces acting on the material, enhancing its lateral movement and ultimately leading to improved die filling. The modeling results presented in Fig. 8 demonstrate the effect of backward pressure on the geometry of the deformed workpiece, die filling, and the plastic strain distribution after SPD. The workpiece-die gap can be observed when backward pressure is less than 50MPa. It is noteworthy that increasing the backward pressure leads to an increase in mean equivalent plastic strain (Fig. 8b). Furthermore, it was found that the standard deviation and the range of the plastic strain were not significantly impacted by the backward pressure. Moreover, the plastic strain distribution pattern changes by changing the backward pressure. While the plastic strain in internal zones increases with backward pressure, it seems that the strains in surface zones are slightly affected. Backward pressure and resultant radial forces push the material radially toward the unfilled gaps, leading to higher strains.

Figure 9 shows the effect of the backward pressure on the extrusion load. As can be seen, by increasing the backward pressure, the extrusion loading curve moves up due to the changes in stress distribution and contact conditions in the die cavity. To gain a deeper insight, the contact pressure distribution on the specimen surface with different backward pressures is presented in Fig. 10. The extrusion in higher backward pressure shows higher contact pressure on the workpiece surface. Notably, the contact pressure in the inlet and twist zones is higher than in the outlet zone. During the extrusion process, the normal pressure and contact traction between the die surface and the workpiece are gradually changed, causing variations in the reverse resistance pressure. As the material enters the twist zone, the applied load increases, and then the load gradually decreases by passing the workpiece through the twist zone (Fig. 9).

The mechanical work in plastic deformation is the sum of ideal work, frictional work, and redundant work (Ref 57). The increase in backward pressure enhances die filling, leading to a larger contact surface, and increased friction traction and work.

Redundant work is mainly attributed to the internal distortion caused by shear deformation and surface friction by twisting in the die. The effects of backward pressure on the extrusion load are not only related to the friction work but also to variations of the internal and redundant works that indirectly contribute to the load. Increasing the plastic strain by increasing the backward pressure leads to a corresponding increase in the internal and redundant works, which ultimately increases the extrusion load.

In the OTE process, the die geometry (i.e., twist zone length, off-axis parameter, and twist angle) plays a crucial role in the deformation behavior of the material during SPD. The effects

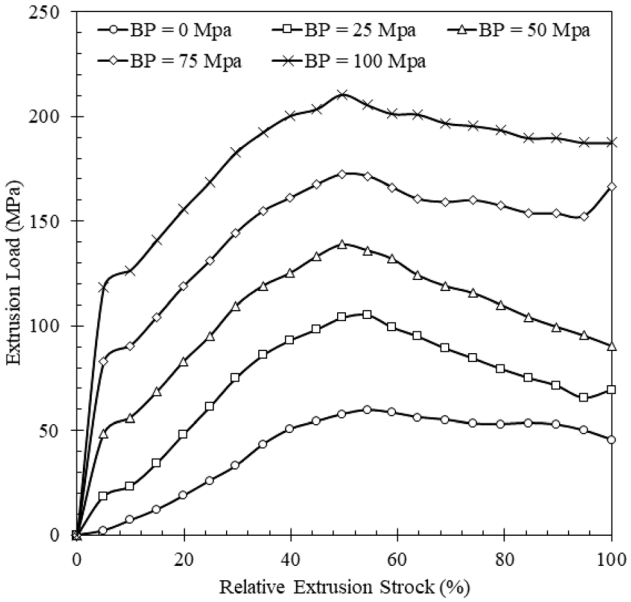

Fig. 9 Calculated extrusion load vs. relative extrusion stroke with different backward pressure (twist angle = 180°)

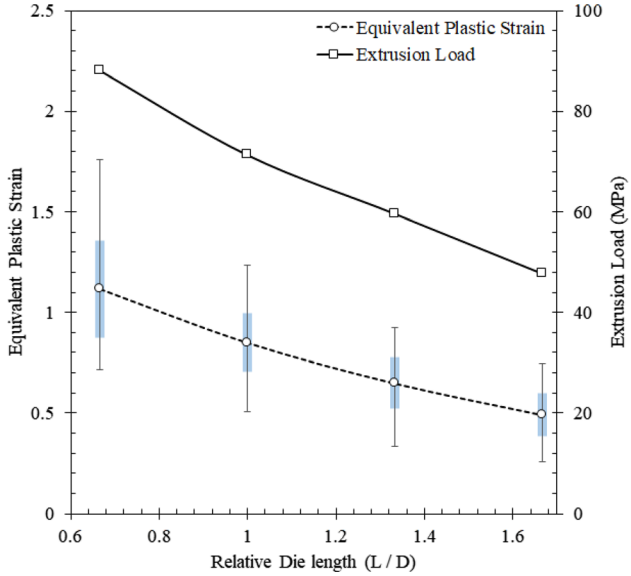

Fig. 11 Effect of twist zone length (*L/D*) on the maximum extrusion load (friction coefficient = 0.07, without BP, twist angle = 180°, length of twist zone = 40mm, and off-center = 3mm)

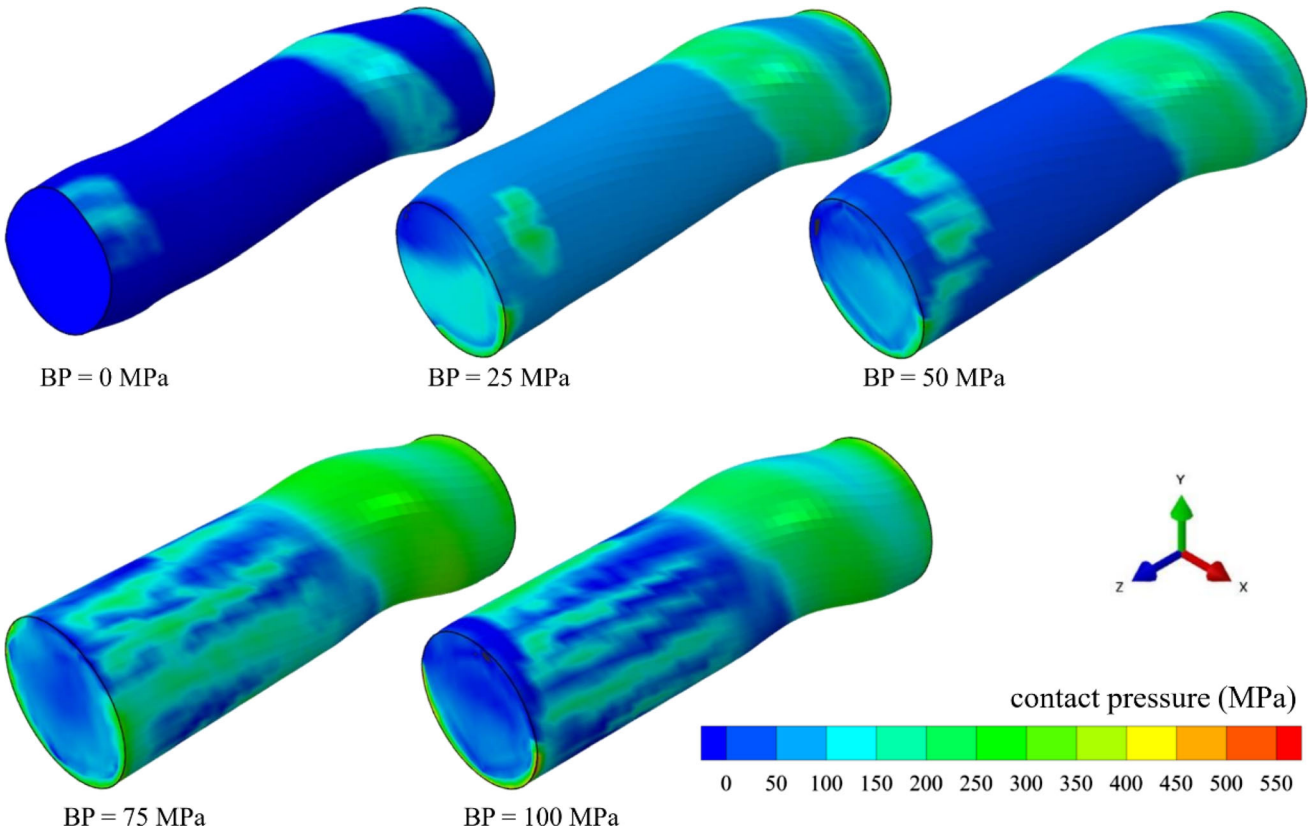

Fig. 10 Distribution of contact pressure on the workpiece surfaces during OTE with different backward (friction coefficient = 0.07, twist angle = 180°, length of twist zone = 40mm, and off-center = 3 mm)

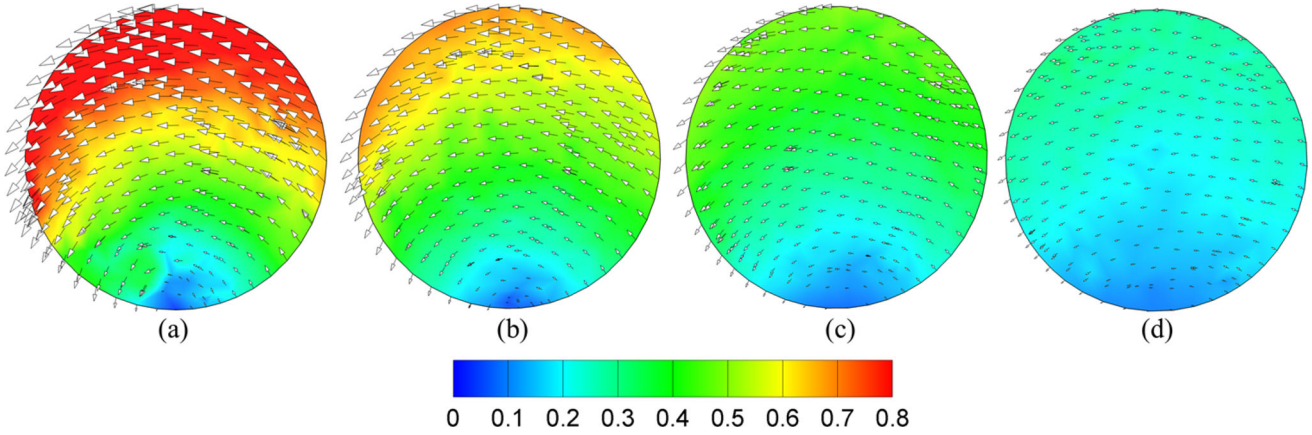

Fig. 12 The velocity distribution at the middle of the twist zone with different off-axis parameters (friction coefficient = 0.07, BP = 100 MPa, twist angle = 180°, length of twist zone = 40mm, cross-section diameter = 15 mm)

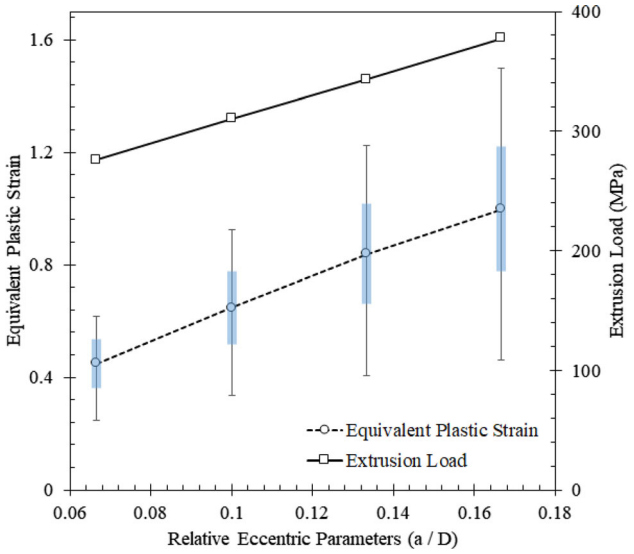

Fig. 13 Effect of the off-axis parameters (a/D) on the maximum extrusion load (friction coefficient = 0.07, BP = 100 MPa, twist angle = 180°, length of twist zone = 40mm, and cross-section diameter = 15mm)

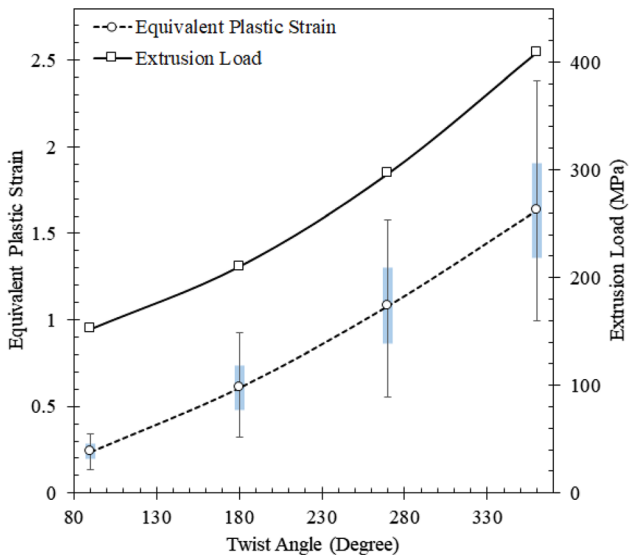

Fig. 14 Effect of the twist angle on the maximum extrusion load (friction coefficient = 0.07, BP = 100 MPa, length of twist zone = 40 mm, cross-section diameter = 15mm, and off-center = 3 mm)

of the twist zone length on extrusion load and applied equivalent plastic strain are illustrated in Fig. 11. It is observed that an increase in L/D ratio (where L and D represent the twist zone length and the diameter of the extrusion channel, respectively) leads to a reduction in the helix angle and, consequently, a decrease in the intensity of the plastic strain applied to the workpiece. As depicted in this figure, an increase in the L/D ratio leads to a decrease in the mean, standard deviation, and range of the equivalent plastic strain, ultimately resulting in a reduction in the extrusion load.

Furthermore, the effect of the off-axis parameter (a/D where a and D are the off-axis and the diameter of the extrusion channel, respectively) on the velocity distribution in the middle of the twist zone is shown in Fig. 12. As can be seen, increasing the off-axis parameter results in an increase in the gradient of the twisting velocity during OTE and consequently an increase in the applied plastic strain (Fig. 15).

The effect of this variable on the maximum extrusion load is presented in Fig. 13. In this figure, the horizontal axis is the ratio of the off-axis parameter (a) to the die diameter (D). As can be seen, an increase in the off-axis parameter results in a rise in the maximum extrusion load. As explained above, an increase in the off-axis parameter leads to an increase in plastic deformation, particularly shear deformation. Therefore, the total power required for extruding the specimen increases, which leads to an increase in the extrusion force.

The effects of twist angle on extrusion load and deformation regime were examined by modeling the OTE process with four different twist angles (90, 180, 270, and 360°). The effect of the twist angle on the extrusion load and the applied plastic strain is presented in Fig. 14. The results in this figure demonstrate a clear correlation between the increase in twist angle and the maximum extrusion load. Increasing the twist angle produces a concomitant rise in the magnitude of plastic strain (Fig. 15) and leads to an increase in the extrusion load.

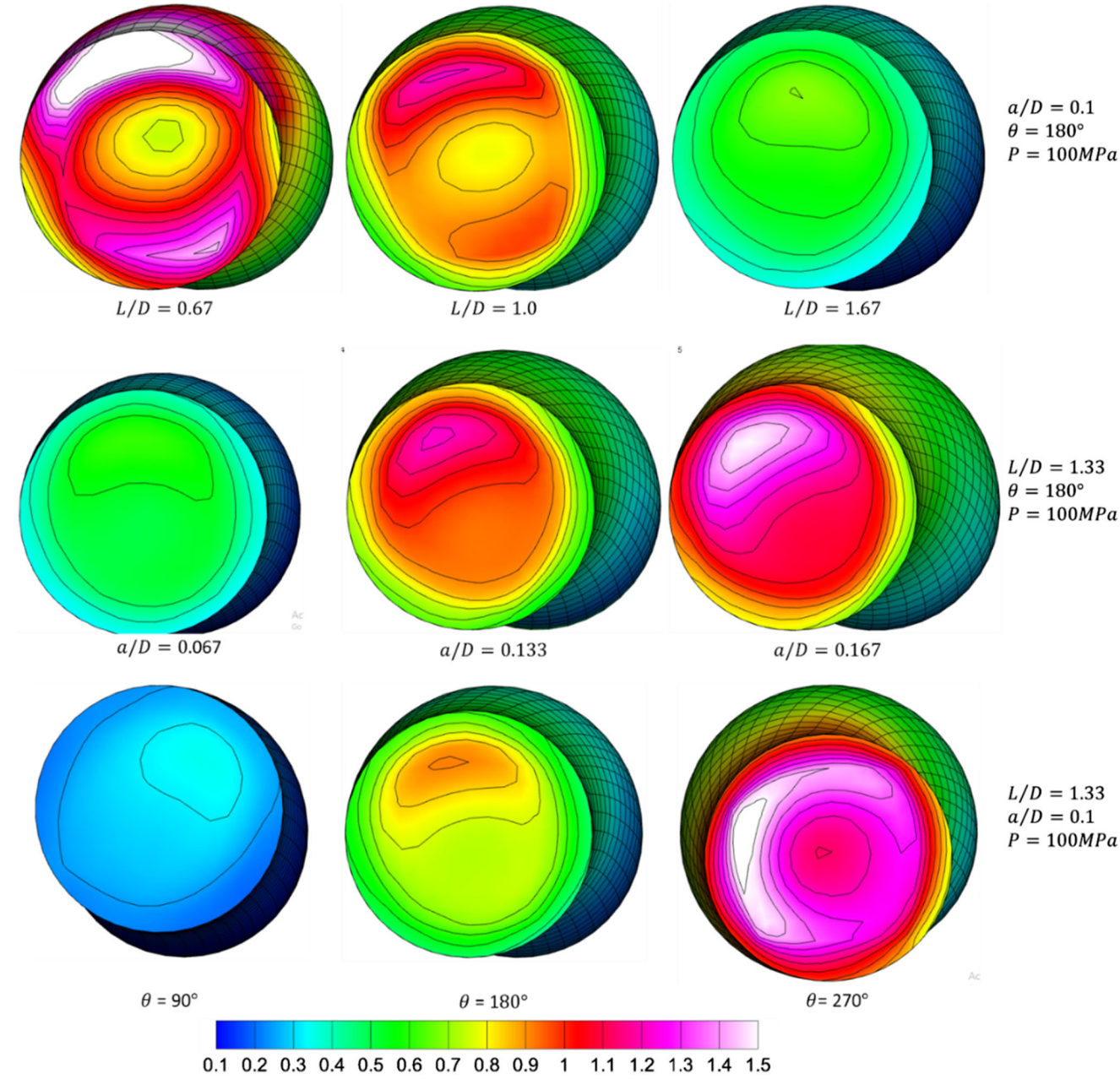

Fig. 15 The distribution of equivalent plastic strain after extrusion with different die geometries

3.3 Microstructural Changes and the Flow Stress During Deformation

In this study, a combined FE and dislocation model is employed to investigate the microstructural characteristics, such as dislocation density and cell sizes, during the OTE process. Figure 16 illustrates the distribution of total dislocation density at the lateral cross section and the cross sections perpendicular to extrusion in the inlet, twist, and outlet zones. Notably, the total dislocation density is significantly increased by passing through the twist zone, and eventually, the dislocation density reaches a constant level in the outlet zone. Furthermore, the surface shear deformation due to frictional surface traction in the inlet zone contributes to an increase in the dislocation density on the surface of the material, which is shown in Fig 16.

Plastic deformation during the movement of the material inside the extrusion die has a significant impact on its microstructural characteristics. To assess the evolution of dislocation cell size and cell wall misorientation angle, the mean and standard deviation of their respective distributions are calculated for a material slice passing through the die. Fig. 17 presents the temporal evolution in the distribution of equivalent plastic strain, cell size, and cell wall misorientation angle during extrusion. The gradual movement and deformation of the material in the die channel lead to an increase in dislocation density, resulting in the formation and refinement of cell structures in the microstructure. As observed, the cell size undergoes a rapid decrease during the initial stages of deformation. Then, it tends to a specific value through the deformation of the material in the twist zone. At higher plastic

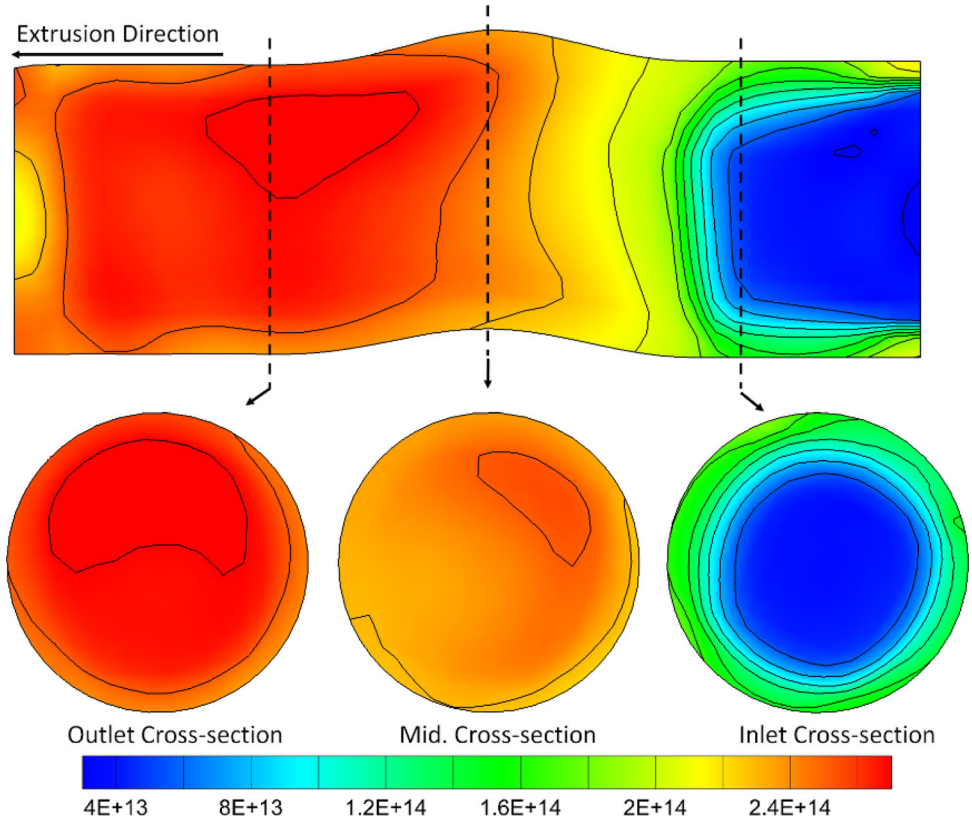

Fig. 16 The distribution of total dislocation density (m^{-2}) at the lateral cross section and the cross sections perpendicular to extrusion in the inlet, twist, and outlet zones (BP = 100 MPa and twist angle = 180°)

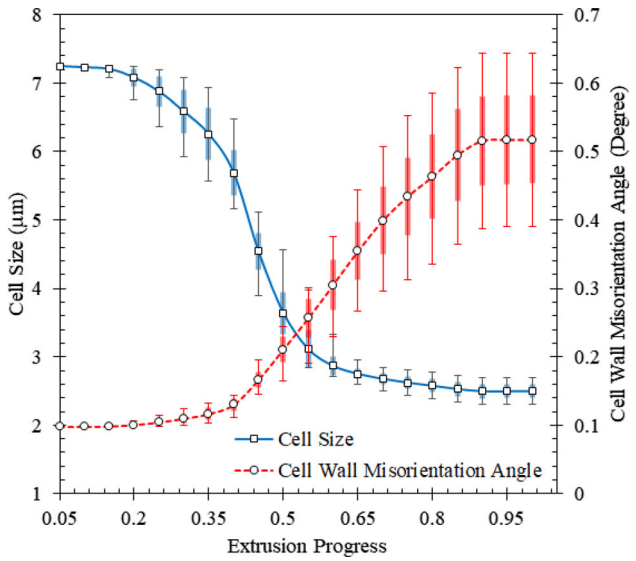

Fig. 17 The temporal evolution in distribution of cell size and cell wall misorientation during extrusion

strains, the cell structures reach a dynamic equilibrium state characterized by almost steady-state cell sizes, as demonstrated in Fig. 5. Also, the misorientation angle of cell walls is increased by increasing the strain applied to the material. The results show that the deformation of the material during extrusion leads to an increase in the standard deviation of the cell wall misorientation angle, indicating a wider distribution of the wall misorientation angle.

By applying the shear plastic deformation, which is followed by decreasing the cell size and increasing the dislocation density, the flow stress of the material is increased. The direct relationship between flow stress and dislocation density is revealed in Eq. 17. Additionally, considering Eq. 12, which displays an inverse correlation between total dislocation density and cell size, it can be concluded that plastic deformation in the OTE process results in work hardening and an increase in material strength. The flow stress distribution at the lateral cross section and cross sections perpendicular to extrusion in the inlet, twist, and outlet zone are presented in Fig. 18. It can be seen that The flow stress increases significantly due to strain hardening as the material is deformed in the twist zone and gradually approaches saturation stress in the outlet zone. Comparing the flow stress distributions in the inlet and the outlet cross sections in Fig. 18 indicates the increase in the yield strength after the OTE processing. Furthermore, the flow stress contour in the inlet cross section in this figure indicates strain hardening in the surface zone of the billet in the inlet container due to frictional deformation. Also, the flow stress is almost homogeneous in the whole middle and outlet cross sections.

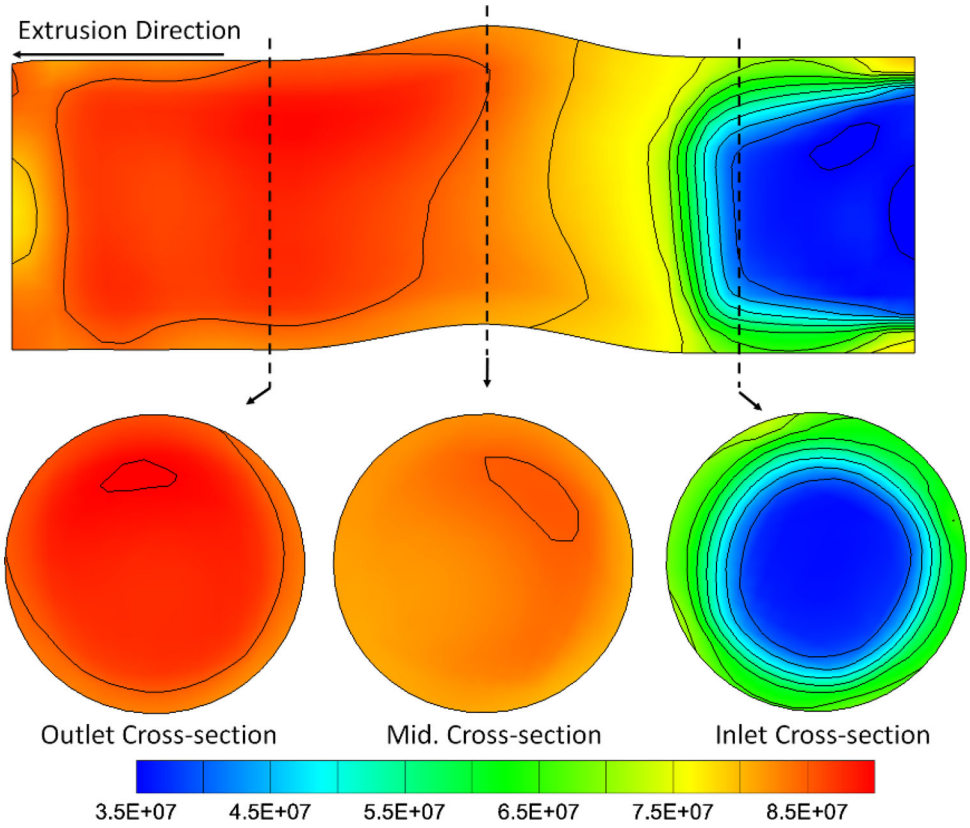

Fig. 18 The flow stress (Pa) distribution at the lateral cross section and cross sections perpendicular to extrusion in the inlet, twist, and outlet zone (BP = 100 MPa and twist angle = 180°)

As discussed in the previous section, both die geometry and extrusion conditions have significant effects on deformation characteristics, the deformation regime, and the dislocation distribution. The influence of twist zone length, the off-axis parameter, the twist angle, and the backward pressure on the distribution of the total dislocation density at the outlet cross section is presented in Fig. 19. As can be seen, the dislocation density decreases by increasing the twist zone length. The increase in twist zone length leads to a decrease in the plastic strain (Fig. 11) and consequently the dislocation density. Another parameter that affects the plastic strain and the dislocation density is the off-axis parameter. An increase in the off-axis parameter leads to an increase in plastic strain (Fig. 12) and the dislocation density. The twist angle also affects the dislocation density. As shown in Fig. 19, increasing the twist angle results in higher plastic strain and dislocation density. Backward pressure also affects the plastic strain distribution and the dislocation density. The dislocation density is increased with increasing the backward pressure.

4. Conclusions

In this study, a combined finite element and dislocation model is used to investigate the microstructural characteristics of pure aluminum during the off-axis twist extrusion process. It is shown that extrusion conditions and die geometry play significant roles in the deformation characteristics, dislocation distribution, cell structure, and material strength. The following concluding remarks can be drawn.

- Backward pressure is a critical variable in eliminating gaps between the workpiece and the die. Increasing the backward pressure enhances the die filling and increases the extrusion load and the mean of equivalent plastic strain.
- The die geometry, twist zone length, off-axis parameter, and twist angle also influence the deformation behavior of the material during TE. Increasing the twist angle and off-axis parameter results in a rise in maximum extrusion load and mean of equivalent plastic strain. However, increasing the L/D ratio results in a decrease in the extrusion load and plastic strain.
- As the material passes through the extrusion die, surface shear deformation caused by severe friction traction contributes to the increase in dislocation density on the surface of the material, even in the inlet zone.
- During initial deformation, cell size rapidly decreases and then stabilizes at higher plastic strains. Increasing the strain leads to an increased misorientation angle of cell walls with a broader distribution.
- The plastic deformation in the OTE process leads to a decrease in cell size and an increase in dislocation density, which increases the flow stress of the material. The flow stress of the material increases significantly due to strain hardening in the twist zone and gradually approaches saturation stress in the outlet zone.

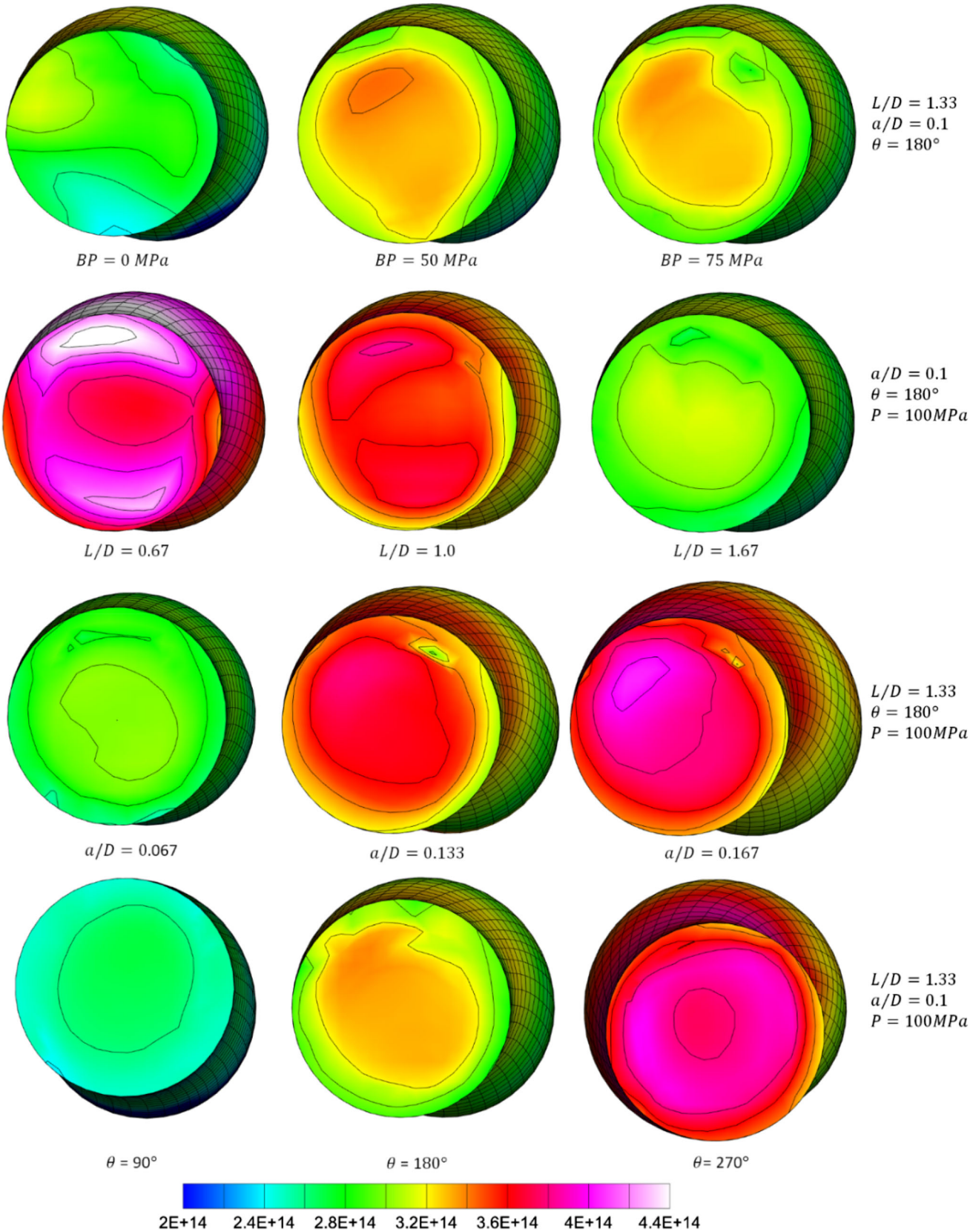

Fig. 19 The distribution of total dislocation density (m^{-2}) after extrusion with different die geometries and backward pressure

- The dislocation density decreases with an increase in the twist zone length, whereas an increase in the backward pressure, off-axis parameter, and twist angle results in an increase in dislocation density.

Conflict of interest

The authors declare that they have no known competing financial interests or personal relationships that could have appeared to influence the work reported in this paper. This research received no specific grant from funding agencies in the public, commercial, or not-for-profit sectors.

References

1. Y. Estrin and A. Vinogradov, Extreme Grain Refinement by Severe Plastic Deformation: A Wealth of Challenging Science, *Acta Mater.*, 2013, **61**(3), p 782–817.
2. R.Z. Valiev, B. Straumal, and T.G. Langdon, Using Severe Plastic Deformation to Produce Nanostructured Materials with Superior Properties, *Annu. Rev. Mater. Res.*, 2022, **52**, p 357–382.
3. K. Edalati, A. Bachmaier, V.A. Beloshenko, Y. Beygelzimer, V.D. Blank, W.J. Botta, K. Bryła, J. Čížek, S. Divinski, and N.A. Enikeev, Nanomaterials by Severe Plastic Deformation: Review of Historical Developments and Recent Advances, *Mater. Res. Letter.*, 2022, **10**(4), p 163–256.
4. C. Wang, F. Li, L. Wang, and H. Qiao, Review on Modified and Novel Techniques of Severe Plastic Deformation, *Sci. China Technol. Sci.*, 2012, **55**(9), p 2377–2390.
5. E.M. Zayed, M. Shazly, A. El-Sabbagh, and N.A. El-Mahallawy, Deformation Behavior and Properties of Severe Plastic Deformation Techniques for Bulk Materials: A Review, *Heliyon*, 2023, **9**, p e16700.
6. Y. Estrin, R. Hellmig, S. Baik, H. Kim, H. Brokmeier, and A. Zi, Microstructure and Texture Development in Copper and Aluminum Under Ecap: New Experimental Results and Modeling, *Ultrafine Grained Mater.*, 2004, **3**, p 247–253.
7. V. Segal, Materials Processing by Simple Shear, *Mater. Sci. Eng. A*, 1995, **197**(2), p 157–164.
8. T.G. Langdon, The Processing of Ultrafine-Grained Materials Through the Application of Severe Plastic Deformation, *J. Mater. Sci.*, 2007, **42**(10), p 3388–3397.
9. N.G. Roy, D. Mondal, P.P. Dey, and M. Ghosh, Equal Channel Angular Pressing (ECAP) with Al Alloy—A Review, *Adv. Mater. Process. Manufact. Appl. Proc. iCADMA*, 2021, **2020**, p 505–513.
10. K. Edalati and Z. Horita, A Review on High-Pressure Torsion (HPT) from 1935 to 1988, *Mater. Sci. Eng. A*, 2016, **652**, p 325–352.
11. Z.-R. Wang, P.-Z. Si, J. Park, C.-J. Choi, and H.-L. Ge, A Review of Ultrafine-Grained Magnetic Materials Prepared by Using High-Pressure Torsion Method, *Materials*, 2022, **15**(6), p 2129.
12. H. Miura, X. Yang, and T. Sakai, Evolution of Ultra-Fine Grains in AZ31 and AZ61 Mg Alloys During Multi Directional Forging and Their Properties, *Mater. Trans.*, 2008, **49**(5), p 1015–1020.
13. Y. Beygelzimer, D. Orlov, A. Korshunov, S. Synkov, V. Varyukhin, I. Vedernikova, A. Reshetov, A. Synkov, L. Polyakov, and I. Korotchenkova, High Pressure Technology of Nanomaterials, *Features of twist extrusion: method, structures & material properties, Solid State Phenomena*. Trans Tech Publ, Stafa, 2006, p 69–78
14. Y. Beygelzimer, D. Prilepo, R. Kulagin, V. Grishaev, O. Abramova, V. Varyukhin, and M. Kulakov, Planar Twist Extrusion Versus Twist Extrusion, *J. Mater. Process. Technol.*, 2011, **211**(3), p 522–529.
15. Y. Beygelzimer, V. Varyukhin, V. Synkov, and S. Synkov, Severe Plastic Deformations of the Materials Under Twist Hydro Extrusion, *Phys. Technol. High Press.*, 2000, **10**(2), p 24.
16. D. Orlov, Y. Beygelzimer, S. Synkov, V. Varyukhin, N. Tsuji, and Z. Horita, Plastic Flow, Structure and Mechanical Properties in Pure Al Deformed by Twist Extrusion, *Mater. Sci. Eng. A*, 2009, **519**(1–2), p 105–111.
17. O. Prokof'eva, Y. Beygelzimer, V.V. Usov, N. Shkatulyak, T.S. Sovkova, A. Sapronov, D. Prilepo, and V. Varyukhin, Formation of a Gradient Structure in a Material by Twist Extrusion, *Russian Metall. (Metally)*, 2020, **2020**, p 573–578.
18. J. Swiostek, J. Göken, D. Letzig, and K. Kainer, Hydrostatic Extrusion of Commercial Magnesium Alloys at 100 C and its Influence on Grain Refinement and Mechanical Properties, *Mater. Sci. Eng. A*, 2006, **424**(1), p 223–229.
19. W. Jurczak, T. Trzepieciński, A. Kubit, and W. Bochnowski, Static and Dynamic Properties of Al-Mg Alloys Subjected to Hydrostatic Extrusion, *Materials*, 2022, **15**(3), p 1066.
20. J. Lee and J. Park, Numerical and Experimental Investigations of Constrained Groove Pressing and Rolling for Grain Refinement, *J. Mater. Process. Technol.*, 2002, **130**, p 208–213.
21. D.H. Shin, J.-J. Park, Y.-S. Kim, and K.-T. Park, Constrained Groove Pressing and its Application to Grain Refinement of Aluminum, *Mater. Sci. Eng. A*, 2002, **328**(1), p 98–103.
22. Y. Saito, N. Tsuji, H. Utsunomiya, T. Sakai, and R. Hong, Ultra-Fine Grained Bulk Aluminum Produced by Accumulative Roll-Bonding (ARB) Process, *Scripta Mater.*, 1998, **39**(9), p 1221–1227.
23. H. Utsunomiya, K. Hatsuda, T. Sakai, and Y. Saito, Continuous Grain Refinement of Aluminum Strip by Conshearing, *Mater. Sci. Eng. A*, 2004, **372**(1), p 199–206.
24. F. Esmaeili, F. Mehri Sofiani, and R. Broomand, A Modified Counterpart of Cyclic Extrusion-Compression: Experimental Study And Dislocation Density-Based Finite Element Modeling, *Proc. Instit. Mech. Eng. Part L J. Mater. Design Appl.*, 2018, **232**(6), p 465–480.
25. H. Sheikh and R. Ebrahimi, Modeling the Effect of Strain Reversal on Grain Refinement and Crystallographic Texture During Simple Shear Extrusion, *Int. J. Solids Struct.*, 2017, **126**, p 175–186.
26. A. Zangiabadi and M. Kazeminezhad, Development of a Novel Severe Plastic Deformation Method for Tubular Materials: Tube Channel Pressing (TCP), *Mater. Sci. Eng. A*, 2011, **528**(15), p 5066–5072.
27. R. Valiev, Nanostructuring of Metals by Severe Plastic Deformation for Advanced Properties, *Nat. Mater.*, 2004, **3**(8), p 511–516.
28. R.Z. Valiev, Y. Estrin, Z. Horita, T.G. Langdon, M.J. Zehetbauer, and Y. Zhu, Producing Bulk Ultrafine-Grained Materials by Severe Plastic Deformation: Ten Years Later, *Jom*, 2016, **68**(4), p 1216–1226.
29. A. Vinogradov and Y. Estrin, Analytical and Numerical Approaches to Modelling Severe Plastic Deformation, *Prog. Mater. Sci.*, 2018, **95**, p 172–242.
30. M. Latypov, I. Alexandrov, Y. Beygelzimer, S. Lee, and H. Kim, Finite Element Analysis of Plastic Deformation in Twist Extrusion, *Comput. Mater. Sci.*, 2012, **60**, p 194–200.
31. M.S. Salehi, N. Anjabin, and H. Kim, An Upper Bound Solution for Twist Extrusion Process, *Met. Mater. Int.*, 2014, **20**(5), p 825–834.
32. C. Wang, F. Li, Q. Li, J. Li, L. Wang, and J. Dong, A Novel Severe Plastic Deformation Method for Fabricating Ultrafine Grained Pure Copper, *Mater. Des.*, 2013, **43**, p 492–498.
33. C. Wang, F. Li, Q. Li, and L. Wang, Numerical and Experimental Studies of Pure Copper Processed by a New Severe Plastic Deformation Method, *Mater. Sci. Eng. A*, 2012, **548**, p 19–26.
34. Y. Beygelzimer, V. Varyukhin, D. Orlov, S. Synkov, Twist Extrusion–Process For Strain Accumulation, *TEAN, Donetsk*, 87 (2003)
35. Y. Beygelzimer, R. Kulagin, M.I. Latypov, V. Varyukhin, and H.S. Kim, Off-Axis Twist Extrusion for Uniform Processing of Round Bars, *Met. Mater. Int.*, 2015, **21**(4), p 734–740.
36. Y. Estrin, L.S. Tóth, A. Molinari, and Y. Bréchet, A Dislocation-Based Model for all Hardening Stages in Large Strain Deformation, *Acta Mater.*, 1998, **46**(15), p 5509–5522.
37. L.S.S. Tóth, A. Molinari, and Y. Estrin, Strain Hardening at Large Strains as Predicted by Dislocation Based Polycrystal Plasticity Model, *J. Eng. Mater. Technol.*, 2001, **124**(1), p 71–77.
38. H. Parvin and M. Kazeminezhad, Development a Dislocation Density Based Model Considering the Effect of Stacking Fault Energy: Severe Plastic Deformation, *Comput. Mater. Sci.*, 2014, **95**(Supplement C), p 250–255.
39. E. Hosseini and M. Kazeminezhad, The Effect of ECAP Die Shape on Nano-Structure of Materials, *Comput. Mater. Sci.*, 2009, **44**(3), p 962–967.

40. E. Hosseini and M. Kazeminezhad, A Hybrid Model on Severe Plastic Deformation of Copper, *Comput. Mater. Sci.*, 2009, **44**(4), p 1107–1115.
41. A. Alyani and M. Kazeminezhad, Mechanistic Modelling of Cryo-Deformation and Post-Annealing of Aluminium, *Mater. Sci. Technol.*, 2023, **39**(4), p 485–495.
42. E. Hosseini and M. Kazeminezhad, Dislocation Structure and Strength Evolution of Heavily Deformed Tantalum, *Int. J. Refract Metal Hard Mater.*, 2009, **27**(3), p 605–610.
43. A. Narooei, G. Roudini, and K. Narooei, Coupling of Bezier-type Streamline and ETMB Model to Predict Dislocation Cell Size in ECAE, *Eng. Res. Exp.*, 2020, **2**(1), 015004
44. K. Romanov, A. Shveykin, and P. Trusov, Advanced Statistical Crystal Plasticity Model: Description of Copper Grain Structure Refinement during Equal Channel Angular Pressing, *Metals*, 2023, **13**(5), p 953.
45. S.M. Hassani-Gangaraj, K. Cho, H.-J. Voigt, M. Guagliano, and C. Schuh, Experimental Assessment and Simulation of Surface Nanocrystallization by Severe Shot Peening, *Acta Mater.*, 2015, **97**, p 105–115.
46. S.S. Kumar and T. Raghu, Structural and Mechanical Behaviour of Severe Plastically Deformed High Purity Aluminium Sheets Processed by Constrained Groove Pressing Technique, *Mater. Des.*, 2014, **57**, p 114–120.
47. E. Hosseini and M. Kazeminezhad, A New Microstructural Model Based on Dislocation Generation and Consumption Mechanisms Through Severe Plastic Deformation, *Comput. Mater. Sci.*, 2011, **50**(3), p 1123–1135.
48. E.M. Viatkina, W.A.M. Brekelmans, and M.G.D. Geers, Modelling of the Internal Stress in Dislocation Cell Structures, *Eur. J. Mech. A. Solids*, 2007, **26**(6), p 982–998.
49. M. Huang, P.E. Rivera-Díaz-del-Castillo, O. Bouaziz, and S. van der Zwaag, A Constitutive Model for High Strain Rate Deformation in FCC Metals Based on Irreversible Thermodynamics, *Mech. Mater.*, 2009, **41**(9), p 982–988.
50. M. Seyed Salehi, N. Anjabin, and H.S. Kim, Study of Geometrically Necessary Dislocations of a Partially Recrystallized Aluminum Alloy Using 2D EBSD, *Microsc. Microanal.*, 2019, **25**(3), p 656–663.
51. L.S. Tóth, Y. Estrin, R. Lapovok, and C. Gu, A Model of Grain Fragmentation Based on Lattice Curvature, *Acta Mater.*, 2010, **58**(5), p 1782–1794.
52. Y. Estrin, L.S. Tóth, Y. Bréchet, and H.S. Kim, Modelling of the Evolution of Dislocation Cell Misorientation Under Severe Plastic Deformation, *Nanomaterials by Severe Plastic Deformation*. Trans Tech Publications Ltd., Stafa, 2006, p 675–680. https://doi.org/10.4028/0-87849-985-7.675
53. Y. Estrin, A. Molotnikov, C. Davies, and R. Lapovok, Strain Gradient Plasticity Modelling of High-Pressure Torsion, *J. Mech. Phys. Solids*, 2008, **56**(4), p 1186–1202.
54. P.W.J. McKenzie, R. Lapovok, and Y. Estrin, The Influence of Back Pressure on ECAP Processed AA 6016: Modeling and Experiment, *Acta Mater.*, 2007, **55**(9), p 2985–2993.
55. A. Rollett, F. Humphreys, G.S. Rohrer, and M. Hatherly, *Recrystallization and Related Annealing Phenomena*, Elsevier, USA, 2004
56. G.J. Raab, R.Z. Valiev, T.C. Lowe, and Y.T. Zhu, Continuous Processing of Ultrafine Grained Al by ECAP–Conform, *Mater. Sci. Eng. A*, 2004, **382**, p 30–34.
57. W.S. Hosford and R.M. Caddell, Metal Forming Mechanics and Metallurgy, *Inc*. Englewood Cliffs, 1983, p 250–255